Journal of Alloys and Compounds 1010 (2025) 177442

Contents lists available at ScienceDirect

Journal of Alloys and Compounds

journal homepage: www.elsevier.com/locate/jalcom

Superconducting properties and electronic structure of $CuAl_2$-type transition-metal zirconide $Fe_{1-x}Ni_xZr_2$

Ryunosuke Shimada [a,b], Yuto Watanabe [a], Lorenzo Tortora [b], Giovanni Tomassucci [b], Muammer Yasin Hacisalihoglu [b,c], Hiroto Arima [a,d], Aichi Yamashita [a], Akira Miura [e], Chikako Moriyoshi [f], Naurang L. Saini [b], Yoshikazu Mizuguchi [a,*]

[a] Department of Physics, Tokyo Metropolitan University, 1-1, Minami-osawa, Hachioji 192-0397, Japan
[b] Dipartimento di Fisica, Universitá di Roma "La Sapienza'', P. le Aldo Moro 2, Roma 00185, Italy
[c] Department of Physics, Recep Tayyip Erdogan University, Rize 53100, Turkey
[d] National Institute of Advanced Industrial Science and Technology, 1-1-1 Umezono, Tsukuba, Ibaraki 305-8563, Japan
[e] Faculty of Engineering, Hokkaido University, Sapporo, Hokkaido 060-8628, Japan
[f] Graduate School of Advanced Science and Engineering, Hiroshima University, Higashihiroshima, Hiroshima 739-8526, Japan

ARTICLE INFO

Keywords:
Superconductivity
Phase diagram
Transition-metal zirconide
Synchrotron XRD
Specific heat

ABSTRACT

$CuAl_2$-type transition-metal (*Tr*) zirconides are a superconductor family, and the *Tr*-site element substitution largely modifies its transition temperature (T_c). Here, we synthesized polycrystalline samples of $Fe_{1-x}Ni_xZr_2$ by arc melting. The crystal structure and the superconducting properties were studied through synchrotron X-ray diffraction, magnetic susceptibility, electrical resistivity, and specific heat measurements. Bulk superconductivity was observed for $0.4 \leq x \leq 0.8$, and the highest T_c of 2.8 K was observed for $x = 0.6$. The obtained superconductivity phase diagram exhibits a dome-shaped trend, which is similar to unconventional superconductors, where magnetic fluctuations are essential for superconductivity. In addition, from the c/a lattice constant ratio analysis, we show the possible relationship between the suppression of bulk superconductivity in the Ni-rich compositions and a collapsed tetragonal transition.

1. Introduction

Transition-metal zirconides with a tetragonal $CuAl_2$-type crystal structure (*I4/mcm*, No. 140) are known as a superconductor family with a variable transition temperature (T_c) depending on the transition-metal (*Tr*) element [1–9]. The highest T_c is 11.3 K in $RhZr_2$ among the $TrZr_2$ family, and the superconducting mechanism is basically understood by phonon-mediated conventional mechanism [8,10]. However, importance of antiferromagnetic spin fluctuation to superconductivity was proposed for $CoZr_2$ [6]. In addition to relatively high T_c, $TrZr_2$ compounds have been drawing much attention to anomalous thermal expansion [9,11–14] and high-entropy material design [13,15,16], in which selection of the *Tr*-site element is essential for physical properties. Therefore, to enrich the knowledge on superconducting properties of $TrZr_2$, further investigation for various combinations of elements at the $TrZr_2$ site is needed.

Among the $TrZr_2$, the number of studies on superconductivity in $FeZr_2$-related samples is limited. In Ref. 3, $Fe_yNi_{1-y}Zr_2$ amorphous metallic-glass samples were investigated for $y \leq 0.6$, and the highest T_c of ~2.6 K was found for $y = 0.1$. Furthermore, magnetism and superconducting properties of Fe-Zr binary phases were systematically studied [17,18]. When z in the $Fe_{1-z}Zr_z$ metallic glass is lower than 0.6, ferromagnetic ordering is observed, and superconductivity is observed for $z > 0.7$. In between the ferromagnetic and superconducting phases, paramagnetic phases are present. Because the Zr concentration in the target phase $TrZr_2$ is 66.7 %, $FeZr_2$ is expected to be located in the vicinity of ferromagnetic and superconducting states in the Fe-Zr binary phase diagram. As well known, superconductivity emerging in the vicinity of magnetic ordering possesses an unconventional mechanism [19]. As mentioned above, $CoZr_2$ may possess collaboration between superconductivity and antiferromagnetic spin fluctuation. Therefore, $FeZr_2$-based superconductors may be potential unconventional superconductors. The previous studies on $FeZr_2$-based materials were performed on glassy samples prepared by a melt-spinning method. In this

* Corresponding author.
E-mail address: mizugu@tmu.ac.jp (Y. Mizuguchi).

https://doi.org/10.1016/j.jallcom.2024.177442
Received 15 July 2024; Received in revised form 16 October 2024; Accepted 6 November 2024
Available online 7 November 2024

study, we aimed to investigate the physical properties of homogeneous samples of $Fe_{1-x}Ni_xZr_2$ by preparing samples using arc melting. A dome-shaped superconductivity phase diagram with the highest T_c of 2.8 K was obtained for polycrystalline samples of $Fe_{1-x}Ni_xZr_2$.

2. Experimental details

Polycrystalline samples of $Fe_{1-x}Ni_xZr_2$ (x = 0, 0.1, 0.2, 0.3, 0.4, 0.5, 0.6, 0.7, 0.8, 0.9, 1.0) were synthesized by arc melting in an Ar atmosphere. Powders of pure transition metals (*Tr*) of Fe (99.9 %, Kojundo Kagaku) and Ni (99.9 %, Kojundo Kagaku) with a nominal composition were mixed and pelletized. The *Tr* pellet and the plates of pure Zr (99.2 %, Nilaco) were used as starting materials. The samples were melted three times and turned over each time for homogenization.

The crystal structure and the purity of the obtained samples were investigated by synchrotron X-ray diffraction (SXRD) at T = 300 K at BL13XU, SPring-8 (proposal No.: 2023A1042).

The SXRD data were collected using MYTHEN system [20] using X-ray with a wavelength of λ = 0.354032 Å. Lattice constants were determined by Rietveld refinement using RIETAN-FP [21], and the schematic image of the crystal structure was drawn using VESTA [22]. The actual compositions of the samples were investigated using energy-dispersive X-ray spectrometry (EDX, Swift-ED, Oxford) on a scanning electron microscope (SEM, TM3030Plus, Hitachi Hightech). We measured randomly selected ten points on the sample surface, and the actual Ni concentration relative to Fe was evaluated by the mean value with standard errors.

XPS measurements were performed on polycrystalline samples of $Fe_{1-x}Ni_xZr_2$ (x = 0, 0.1, 0.2, 0.3, 0.4, 0.5, 0.6, 0.7, 0.8, 0.9, 1.0) at room temperature using the in-house UHV system at the Sapienza University of Rome, equipped with a double-anode XR50 X-ray source and an AR125 Omicron electron analyzer. The base pressure during the measurements was ~3 × 10^{-9} mbar. The Al $K\alpha$ emission line ($h\nu$ = 1486.6 eV) was used to measure core-level XPS. The X-ray incident and photoelectron emission angles were ~45 deg. for the measurements. The sample surfaces were repeatedly scraped *in situ* by a diamond file to obtain clean surfaces.

The temperature dependences of magnetic susceptibility ($4\pi\chi$) were measured using a superconducting quantum interference device (SQUID) magnetometer (MPMS3, Quantum Design) after both zero-field cooling (ZFC) and field cooling (FC) with an applied field of 1 mT. Temperature and magnetic-field dependences of electrical resistivity (ρ) and specific heat (C) measurements were performed using a physical property measurement system (PPMS Dynacool, Quantum Design) equipped with a 9 T superconducting magnet. Electrical resistivity was measured by a four-probe DC method using silver paste and gold wires for the contact between a polished rectangular cuboid sample and sample puck. The measurement was performed using an excitation current of 1 mA. The C measurement was carried out by means of a thermal relaxation method. The sample was mounted on a stage with N-grease for good thermal connection.

3. Results and discussion

Fig. 1(a) shows the SXRD patterns for x = 0–1.0. These compounds have a tetragonal $CuAl_2$-type structure (*I4/mcm*, No. 140), and the main peaks could be indexed with the tetragonal structural model. The peaks systematically shift by Ni substitution. Fig. 1(c) shows the schematic images of the crystal structure of $Fe_{1-x}Ni_xZr_2$. Small impurity peaks of the orthorhombic $FeZr_3$ (or (Fe,Ni)Zr_3) phase (*Cmcm*, No. 63) are seen as shown in Fig. 1(b); for x = 0.6, the $FeZr_3$ impurity ratio obtained from the two-phase analysis was 11.9 wt%. Rietveld refinement results for

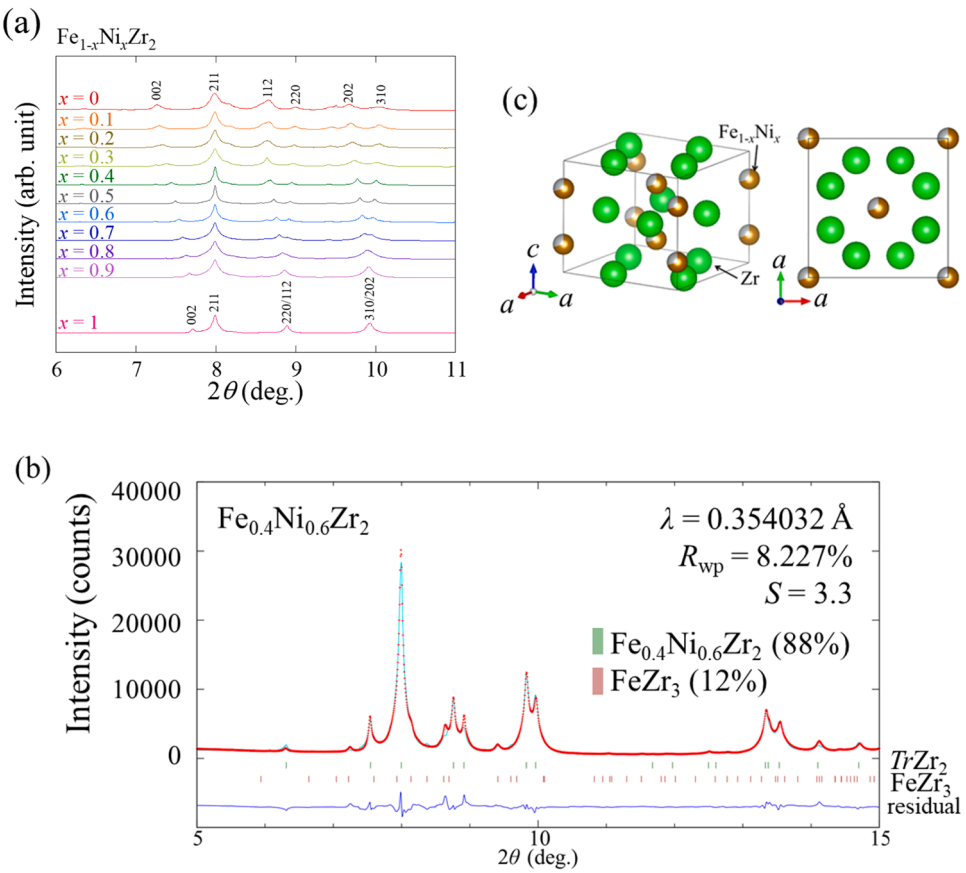

Fig. 1. (a) Powder Synchrotron X-ray diffraction patterns of $Fe_{1-x}Ni_xZr_2$. The numbers are Miller indices. (b) Rietveld refinement result for x = 0.6. (c) Schematic images of crystal structure of $Fe_{1-x}Ni_xZr_2$. The impurity contents are shown as mass fraction.

other compositions are shown in Fig. S1. We estimated lattice constants a and c by the two-phase Rietveld refinements using the SXRD patterns at 300 K, and the obtained x dependence of lattice constants are plotted in Fig. 2(a). The Ni concentrations are obtained using EDX. The obtained actual compositions at the *Tr* site which was measured using EDX are comparable to the nominal values as shown in Fig. 3. The x dependences of the lattice constants are consistent with the shift of the corresponding SXRD peak positions; hence, the influence of the impurity phases is almost negligible in the evaluation of the changes in lattice constants.

Fig. 4(a) shows the XPS spectra for Fe-2p and Ni-2p core levels for all the examined samples. We fit the peaks to estimate the compositional ratio of Fe and Ni. The estimated Ni concentration is plotted as a function of nominal x in Fig. 4(b). As indicated by the solid line, which is the ideal value from the nominal compositions, the trend of the estimated Ni concentration is consistent with the nominal values, which suggests a successful Ni/Fe solution in the examined samples.

Fig. 5(a) shows temperature dependences of magnetic susceptibility ($4\pi\chi$) normalized at $T = 4$ K of $Fe_{1-x}Ni_xZr_2$ measured in ZFC process. As shown in Fig. S2, negative background was observed in some compositions when the applied field is low. Therefore, to discuss the evolution of superconducting signals, we normalized the data at $T = 4$ K. We observed a superconducting transition at $T_c = 2.2$, 2.6, 2.7, 2.6, 2.4, 1.9, and 2.0 K for $x = 0.4$, 0.5, 0.6, 0.7, 0.8, 0.9, and 1, respectively. There is no multiple-step superconducting transition in the temperature dependence for these compositions between 1.8 and 10 K, which is another proof of homogeneous (systematic) Ni substitution in $Fe_{1-x}Ni_xZr_2$. The large diamagnetic signals observed for $0.4 \leq x \leq 0.8$ suggests the emergence of bulk superconductivity. In contrast, the signals for $x > 0.8$ are clearly small as a bulk superconductor, which indicates that the observed diamagnetic signals are caused by filamentary (trace) superconductivity states in those samples. Above 1.8 K, no superconductivity was observed for $0 \leq x \leq 0.3$. Bulk superconductivity was first observed at $x = 0.4$, and T_c increased until $x = 0.6$. The highest T_c of 2.7 K was observed for $x = 0.6$. However, for $x > 0.6$, the T_c tends to decrease with increasing x. Fig. 6 shows the x dependence of T_c, in which a dome-shaped superconductivity phase diagram was observed. Here, we briefly discuss the normal-state magnetic properties. Fig. S2(a) shows the $4\pi\chi(T)$ measured after FC and ZFC under $\mu_0H = 1$ mT for $Fe_{1-x}Ni_xZr_2$. Large diamagnetic signals other than superconductivity were observed for $0.3 \leq x \leq 0.6$. As shown in Fig. S2(b), its large diamagnetism was observed for $x = 0.5$ from 1.8 K to 300 K. Fig. S2(c) shows the hysteresis loop (M-H loop) for $x = 0.5$ at $T = 300$ K. The diamagnetic signals were observed up to $\mu_0H = +5$ mT, but turns from negative to positive when a magnetic field higher than about $\mu_0H = +5$ mT was applied. At present, we cannot conclude the origins of the diamagnetic signals, studies on

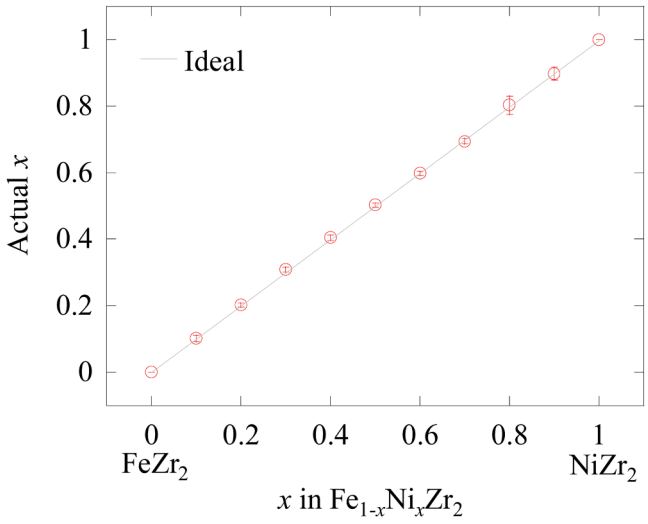

Fig. 3. EDX analysis result: nominal x dependence of actual x in $Fe_{1-x}Ni_xZr_2$. Solid line represents an ideal line when actual x equals nominal x.

single crystals will be needed. Fig. S3 shows the $M(T)$ under $H = 0.1$ T for $Fe_{1-x}Ni_xZr_2$. As can be seen in Figs. S2(b) and S3(f), the $M(T)$ for $x = 0.5$ depends on the applied H, with convex downward and upward behavior under 1 mT and 0.1 T, respectively. In Fig. S3(k), a antiferromagnetic-like anomaly was observed at $T \sim 50$ K. It is possible that the samples with $x > 0.8$ exhibit filamentary superconductivity due to the emergence of antiferromagnetism. The dome-shaped superconductivity phase diagram and the possible antiferromagnetic fluctuations at the vicinity of $NiZr_2$ may be caused by unconventional superconductivity linked with spin fluctuations. However, further investigations on single crystals are needed to conclude the mechanism.

The $\rho(T)$ for the sample of $Fe_{1-x}Ni_xZr_2$ ($x = 0$, 0.5, 0.6, 0.7, 0.8, 1) under $\mu_0H = 0$ T are shown in Fig. 7(a)–(f). At low temperatures, a drop of ρ to zero was observed for $x = 0.5$–0.8, which indicates a superconducting transition. The zero resistivity was observed at $T_c^{zero} = 2.6$, 2.8, 2.5, and 2.4 K for $x = 0.5$, 0.6, 0.7, and 0.8, respectively. The T_c obtained from the zero-resistivity temperature agreed with that estimated from the magnetic susceptibility. The $\rho(T)$ exhibits a metallic behavior in a normal state for all samples. In the low-temperature normal-state regime, the $\rho(T)$ curve can be fitted using the power-law model: $\rho(T) = \rho_0 + AT^{n_{PL}}$, where ρ_0, A, and n_{PL} are residual resistivity, temperature-independent coefficient, and power exponent, respectively. The $\rho(T)$ curve at $T = 4$–80 K was fitted using the model,

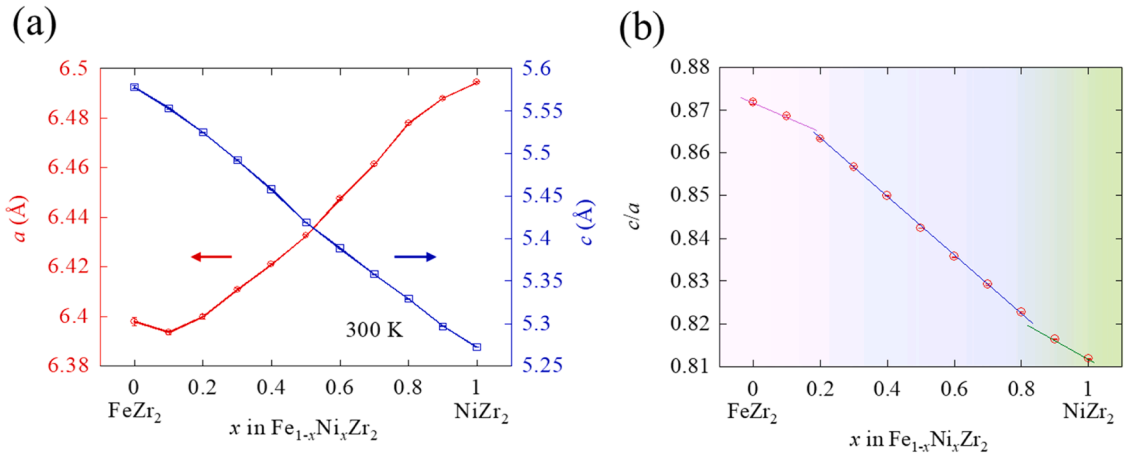

Fig. 2. Ni concentration dependences of lattice constants (a) a and c, and (b) c/a ratio of $Fe_{1-x}Ni_xZr_2$. The error bars are standard deviations estimated by the Rietveld refinement.

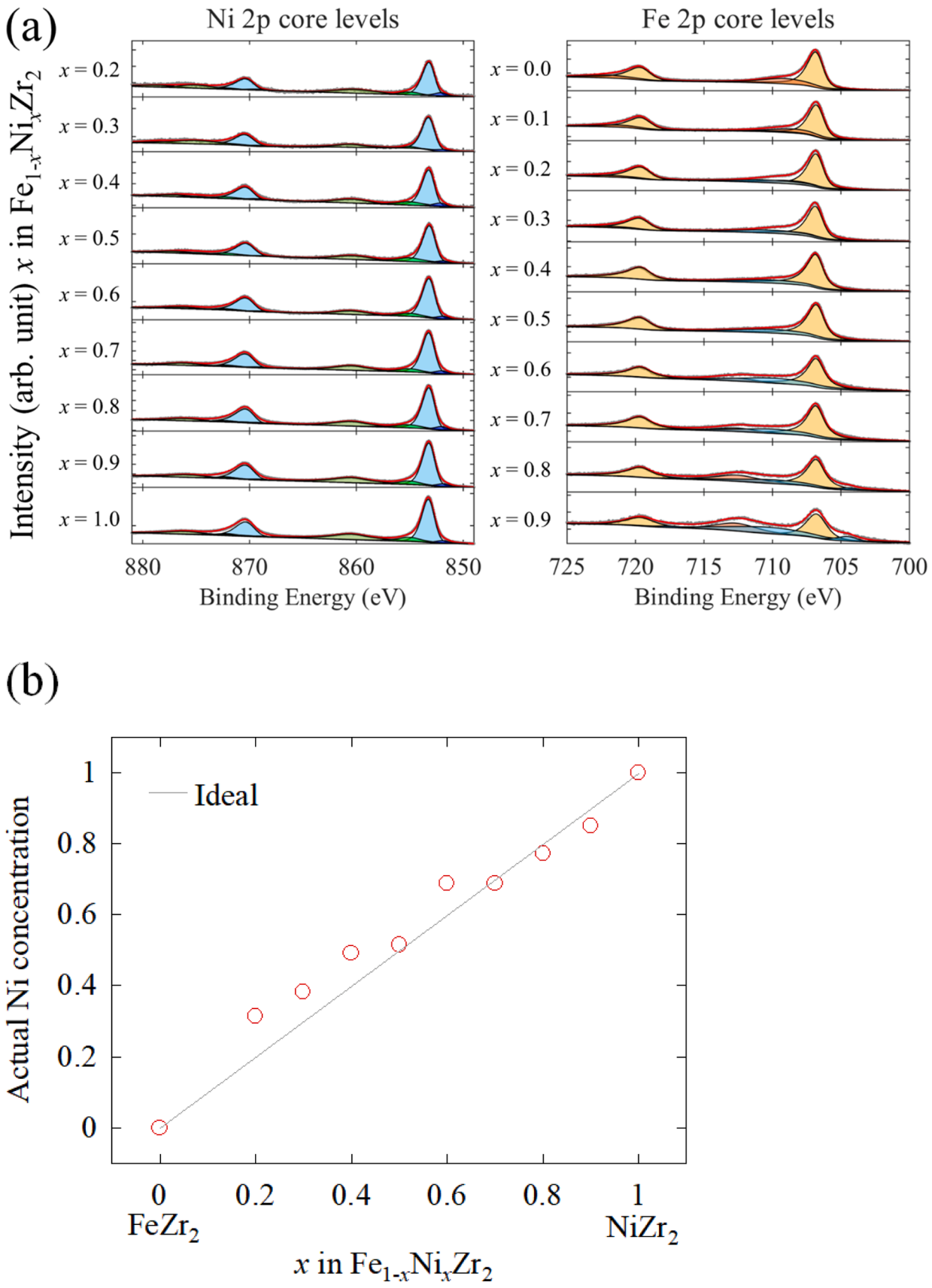

Fig. 4. (a) XPS spectra for Fe-2p and Ni-2p core levels. (b) Ni concentration estimated from the XPS analysis. Solid line represents an ideal line when actual x equals nominal x.

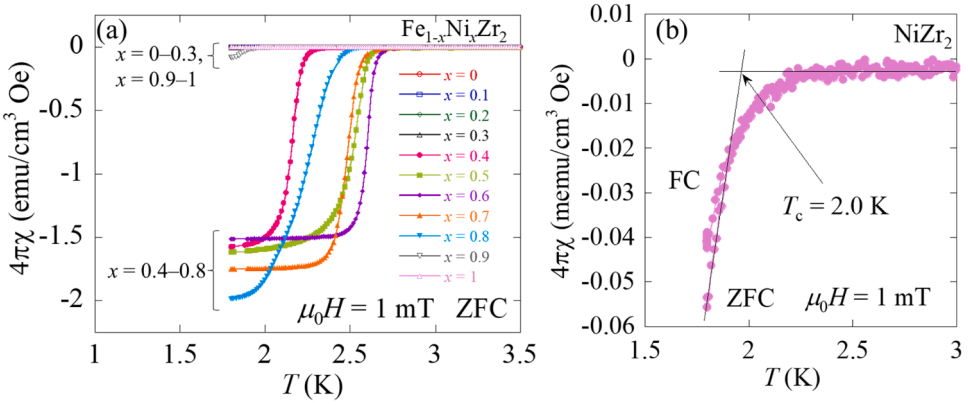

Fig. 5. (a) Temperature dependences of magnetic susceptibility of $Fe_{1-x}Ni_xZr_2$ normalized at 4 K. (b) Enlarged view near T_c for x = 1.0.

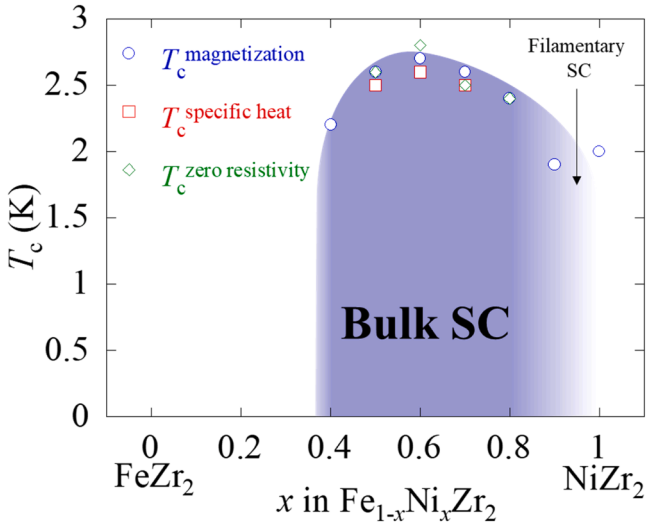

Fig. 6. Superconductivity phase diagram of $Fe_{1-x}Ni_xZr_2$.

with ρ_0 = 0.015, 0.45, 0.27, 0.11, 0.28, and 0.0067 mΩ cm, A = 0.000016, 0.00008, 0.00013, 0.00008, 0.00019, and 0.0000024 mΩK^{-2}, and n_{PL} = 1.9, 1.5, 1.3, 1.3, 1.4, and 2.0 for x = 0, 0.5, 0.6, 0.7, 0.8, and 1, respectively. The fitted curves using the power-law model are displayed as dashed lines in Fig. 7(a)–(f). ρ at 300 K, $\rho_{300\ K}$, is 0.28, 0.54, 0.43, 0.19, 0.52, and 0.06 for x = 0, 0.5, 0.6, 0.7, 0.8, and 1, respectively. Residual resistivity ratio, RRR = $\rho_{300\ K}/\rho_0$, is 19, 1.2, 1.6, 1.7, 1.8, and 8.9 for x = 0, 0.5, 0.6, 0.7, 0.8, and 1, respectively. Undoped $FeZr_2$ and $NiZr_2$ showed relatively large RRR like $CoZr_2$ [4,13]. In contrast, the doped (solid-solution) samples showed smaller RRR values, which would be caused by the disorder due to the elemental substitution.

To further confirm the bulk nature of the observed superconducting transitions for the samples of $Fe_{1-x}Ni_xZr_2$ (x = 0, 0.4, 0.5, 0.6, 0.7, 0.8, 0.9, 1), C measurements were performed. Fig. 8(a)–(h) show the squared-temperature (T^2) dependences of the total $C(T)/T$ under 0 and 9 T. A clear jump was observed for x = 0.4–0.8 under 0 T, which indicates the bulk nature of their superconducting transitions. No bulk superconducting transition was detected by C for x = 0, 0.9, and 1.0 under 0 T above 1.8 K. The $C(T)/T$ data under 9 T were fitted to $C(T)/T = \gamma + \beta T^2$, where γ and β are Sommerfeld coefficient and the coefficient for the phonon contribution to total specific heat, respectively. The estimated γ were 18.32(2), 19.68(4), 21.02(4), 19.43(5), 19.45(4), 18.10(7), 15.56(5), and 16.03(7) mJ K^{-2} mol^{-1}, and β were 0.327(1), 0.438(2), 0.466(2), 0.466(3), 0.480(2), 0.478(4), 0.457(3), and 0.423 (4) mJ K^{-4} mol^{-1} for x = 0, 0.4, 0.5, 0.6, 0.7, 0.8, 0.9, and 1, respectively. Debye temperature Θ_D can be calculated using the β and the formula $\Theta_D = \left(\frac{12\pi^4 NR}{5\beta}\right)^{1/3}$, where N = 3 is the number of atoms per formula unit and R = 8.31 J K^{-1} mol^{-1} is an ideal gas constant. The calculated Θ_D were 261, 237, 232, 232, 230, 230, 234, and 240 K for x = 0, 0.4, 0.5, 0.6, 0.7, 0.8, 0.9, and 1, respectively. Temperature dependences of the electron contribution of the specific heat $C_{el}(T)$ estimated by subtracting phonon contributions βT^3 from $C(T)$ are shown in Fig. 8(i)–(k) for x = 0.5, 0.6, and 0.7, respectively. T_c determined from $C_{el}(T)$ under 0 T was 2.5 K, 2.6 K, and 2.5 K for x = 0.5, 0.6, and 0.7, respectively. The normalized jumps of $C_{el}(T)$, $\Delta C_{el}/\gamma T_c$, were estimated as 1.28, 1.30, and 1.35 for x = 0.5, 0.6, and 0.7, respectively. The values of the jump magnitude were similar and slightly lower than 1.43, which is the value expected by the weak-coupling BCS theory [23]. This result suggests that $Fe_{1-x}Ni_xZr_2$ (x = 0.5, 0.6, 0.7) are fully-gapped superconductors. When assuming electron-phonon coupling superconductivity, we can calculate an electron-phonon coupling constant $\lambda_{el\text{-}ph}$ using the McMillan formula [24]: $\lambda_{el-ph} = \frac{1.04+\mu^* \ln\left(\frac{\Theta_D}{1.45T_c}\right)}{(1-0.62\mu^*)\ln\left(\frac{\Theta_D}{1.45T_c}\right)-1.04}$, where μ^* = 0.13 is a Coulomb coupling constant and the value is used empirically for similar materials containing transition metals. We obtained the values of $\lambda_{el\text{-}ph}$ to be 0.57 for x = 0.5, 0.6, and 0.7. Sommerfeld coefficient (γ) is proportional to the electronic density of states at the Fermi energy $D(E_F)$ and a term $(1 + \lambda_{el\text{-}ph})$ from the electron-phonon interaction. Therefore, $D(E_F)$ with spin degeneracy can be expressed in $D(E_F) = \frac{3\gamma}{\pi^2 k_B^2 (1+\lambda_{el-ph})}$. The measured γ and calculated $\lambda_{el\text{-}ph}$ provide $D(E_F)$ = 5.70 states eV^{-1} per formula unit (f.u.), 5.24 states eV^{-1} per f.u., and 5.27 states eV^{-1} per f.u. for x = 0.5, 0.6, and 0.7, respectively. T_c does not increase with an increase in Θ_D or γ, unlike the explanation in the BCS theory.

Fig. 9(a) and (b) show temperature dependences of total specific heat $C(T)$ and electric resistivity $\rho(T)$ at several magnetic fields for x = 0.6, respectively. Magnetic fields were applied with an increment of 0.2 T up to μ_0H = 1 T and also measured at μ_0H = 9 T for $C(T)$. For $\rho(T)$, the magnetic fields are increased by 0.2 T up to μ_0H = 2 T. Fig. 9(c) is the temperature dependences of upper critical field $\mu_0H_{c2}(T)$ for x = 0.6. The data points were taken from temperature dependences of $\rho(T)$ with 50 % criterion, and $C(T)$ under several magnetic fields. The upper critical field at 0 K, $\mu_0H_{c2}(0)$ can be calculated by fitting the data using the Ginzburg-Landau (GL) model [24,25]: $\mu_0H_{c2}(T) = \mu_0H_{c2}(0)\left[\frac{1-(T/T_c)^2}{1+(T/T_c)^2}\right]$. We obtained the value of $\mu_0H_{c2}(0)$ for x = 0.6 to be 4.03 T for $\rho(T)$ 50 % criterion, and 4.28 T for $C(T)$. We found that the whole values of $\mu_0H_{c2}(0)$ were lower than that of μ_0H_P = 5.51 T calculated with T_c of $\rho(T)$ 50 % criterion using the following formula: $\mu_0H_P = \frac{\Delta(0)}{\sqrt{g}\mu_B} = 1.86T_c$, where g = 2 is a g-factor for free electron and $\mu_B \approx 9.27\times10^{-24}$ J T^{-1} is a Bohr magneton. The $\Delta(0)$ is a superconducting gap energy at 0 K described as

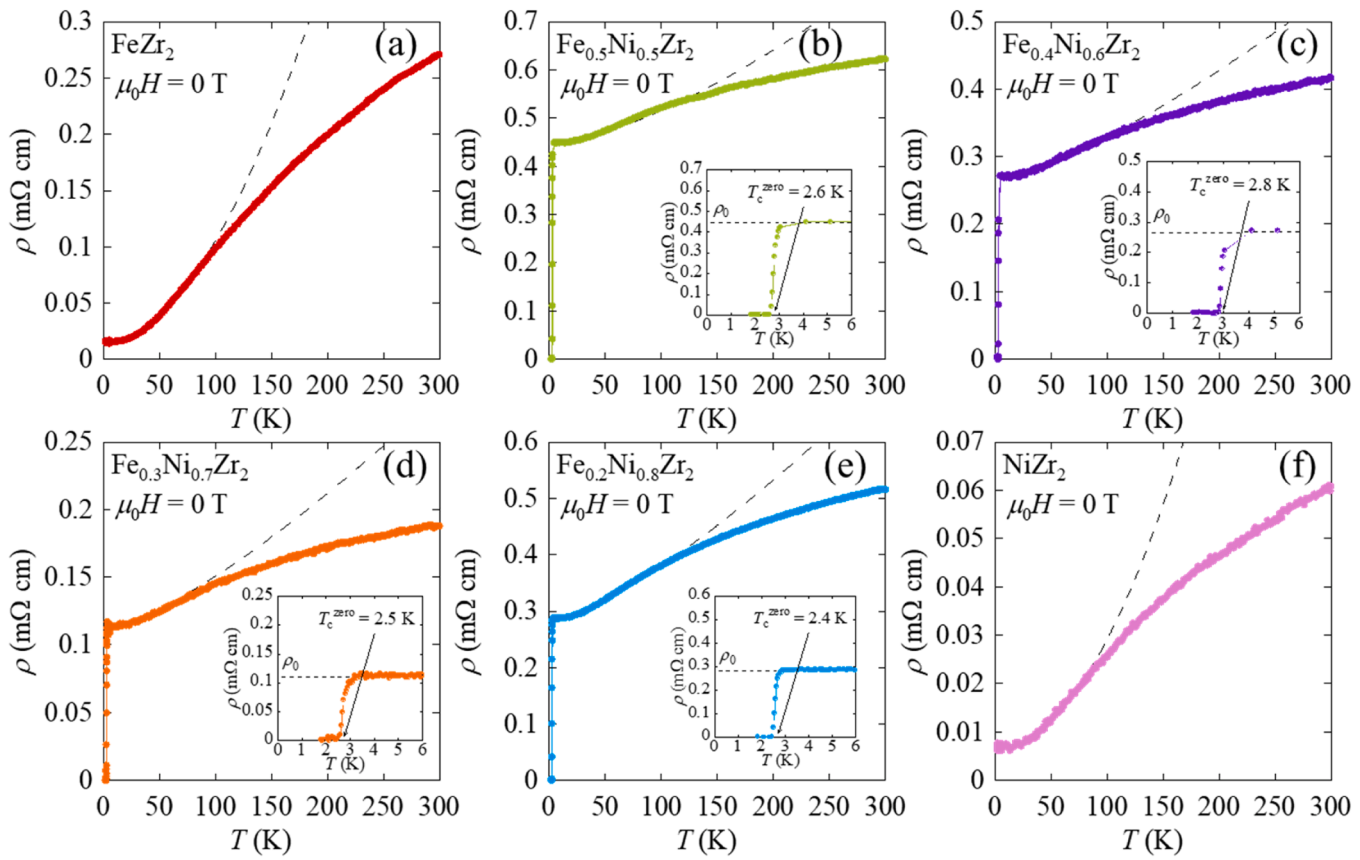

Fig. 7. ((a)–(f)) Temperature dependences of electrical resistivity under 0 T for $Fe_{1-x}Ni_xZr_2$ (x = 0, 0.5, 0.6, 0.7, 0.8, 1). The insets are enlarged view near T_c. The dashed lines are fit to power-law model.

$\Delta(0) = 1.76k_BT_c$ ($k_B \approx 1.38\times10^{-23}$ J K^{-1} is a Boltzmann constant) in the single gap Bardeen−Cooper−Schrieffer (BCS) model [23].

For $x \leq 0.3$, $x \geq 0.9$, the bulk nature of superconductivity is suppressed. To explore a possible cause of the suppression of superconductivity, we estimated the c/a ratio of $Fe_{1-x}Ni_xZr_2$ using the SXRD data and plotted in Fig. 2(b) as a function of x. In $Co_{1-x}Ni_xZr_2$, a collapsed tetragonal transition was observed in a Ni-rich region, and the bulk nature of superconductivity is suppressed after the collapsed tetragonal transition [9]. In the case of the current system, although c/a linearly decreases with increasing x, the slope clearly changes at around x = 0.1–0.3 and x = 0.7–0.9. For x = 0–0.1 and x = 0.9–1, another slope can guide the evolution of c/a. We consider that the change in the c/a ratio in the Ni-rich region is a kind of transition to the collapsed tetragonal phases as revealed in $Co_{1-x}Ni_xZr_2$. Similar collapsed tetragonal transitions were observed in iron-based superconductors $CaFe_2As_2$ and KFe_2As_2 and related layered compounds [26–31]. The electronic structure is generally affected by the collapsed tetragonal transition, which affects superconductivity as well [32,33]. In Fig. 7, there is a difference in the magnitude of RRR between the undoped and doped samples, and the slope of the x dependence of c/a ratio changes in the Fe-rich and Ni-rich regions. The low RRR and *Tr*-site disorder may be linked to the collapsed tetragonal phases, but further experiments using single crystals are needed for concluding the correlation. On the absence of bulk superconductivity in the Fe-rich region, we have no explanation at present, but we assume that the disappearance of bulk superconductivity would be related to strong spin fluctuations and/or the transition to a collapsed tetragonal phase. To clarify that, further structural, electronic, and magnetic properties should be investigated.

4. Summary

We newly synthesized polycrystalline samples of the transition-metal zirconide $TrZr_2$ superconductor $Fe_{1-x}Ni_xZr_2$ by arc melting. From SXRD and XPS measurements, the systematic Fe/Ni solutions were confirmed. Bulk superconductivity was confirmed for $0.4 \leq x \leq 0.8$ from the magnetic susceptibility, electrical resistivity, and specific heat measurement, and the highest T_c of 2.8 K was observed for x = 0.6. In addition, for $NiZr_2$, antiferromagnetic-like anomaly was observed. Having considered the dome-shaped superconductivity phase diagram and the presence of 3d electrons come from magnetic elements of Fe and Ni with the possible magnetic ordering, we assume that the superconductivity in $Fe_{1-x}Ni_xZr_2$ is linked to spin fluctuations, but further experiments are required to address the possible correlation. The upper critical field was determined from electrical resistivity and specific heat data under several magnetic fields; the upper critical field for $Fe_{0.4}Ni_{0.6}Zr_2$ is $\mu_0H_{c2}(0)$ = 4.03 T. From c/a ratio analysis, the suppression of bulk superconductivity in the Ni-rich compositions is ascribed as the collapsed tetragonal transition.

CRediT authorship contribution statement

Yuto Watanabe: Writing – review & editing, Validation, Supervision, Methodology, Investigation, Formal analysis, Data curation. **Lorenzo Tortora:** Writing – review & editing, Visualization, Validation, Supervision, Methodology, Investigation, Formal analysis, Data curation. **Yoshikazu Mizuguchi:** Writing – review & editing, Writing – original draft, Visualization, Validation, Supervision, Resources, Project administration, Methodology, Investigation, Funding acquisition, Formal analysis, Data curation, Conceptualization. **Ryunosuke Shimada:** Writing – review & editing, Writing – original draft,

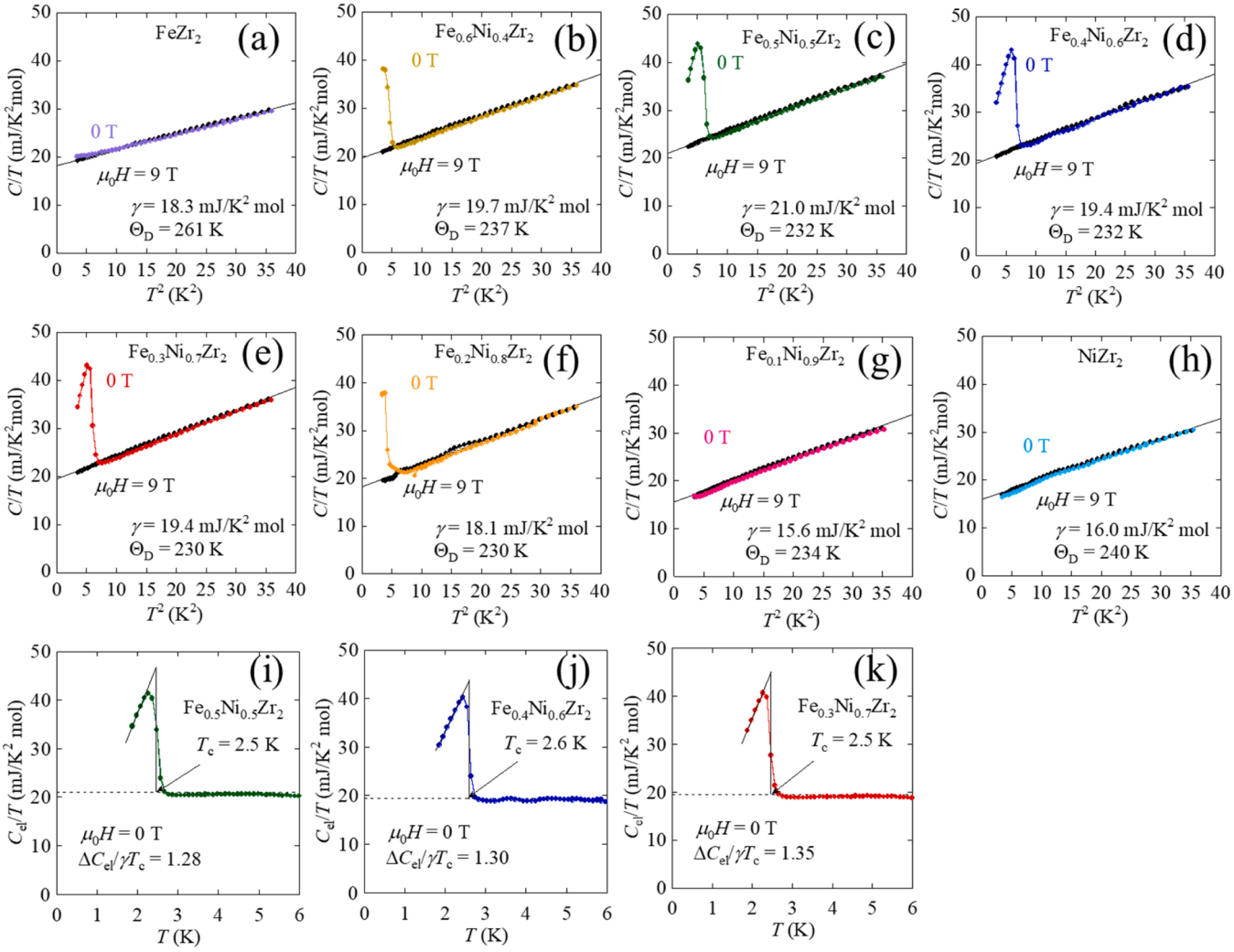

Fig. 8. ((a)–(h)) Squared-temperature (T^2) dependences of total specific heat under 0 and 9 T in the form of $C(T)/T$ for $Fe_{1-x}Ni_xZr_2$ (x = 0, 0.4, 0.5, 0.6, 0.7, 0.8, 0.9, 1). The solid lines are fit to $C(T)/T = \gamma + \beta T^2$. ((i)–(k)) Temperature dependences of electronic specific heat under 0 T for x = 0.5, 0.6, 0.7. The solid lines are used to estimate T_c and dashed lines represent γ value.

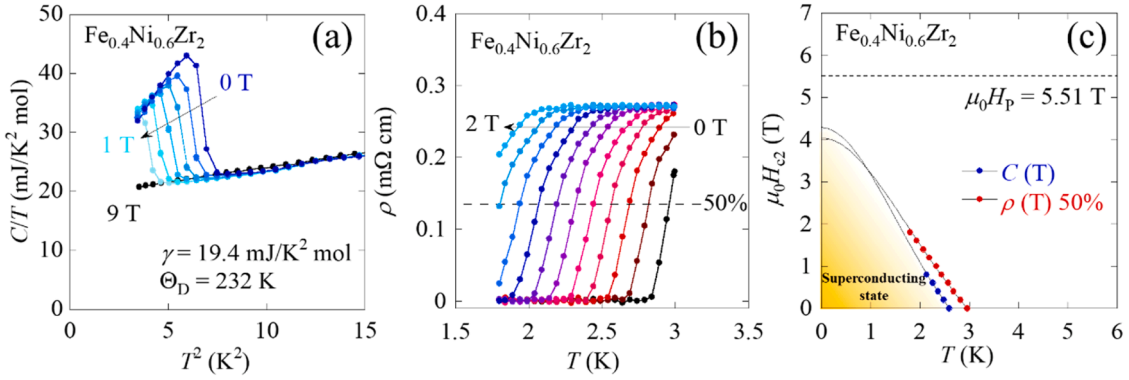

Fig. 9. Temperature dependences of (a) total specific heat and (b) electrical resistivity under several magnetic fields for $Fe_{0.4}Ni_{0.6}Zr_2$. The dashed line represents the 50 % criterion to determine temperature dependence of the upper critical field. (c) Temperature dependence of upper critical field for $Fe_{0.4}Ni_{0.6}Zr_2$. The solid lines are fit to the GL model. The value of μ_0H_P was calculated using $\mu_0H_P = 1.86T_c$ with $\rho(T)$ 50 % criterion data.

Visualization, Validation, Methodology, Investigation, Formal analysis, Data curation, Conceptualization. **Chikako Moriyoshi:** Writing – review & editing, Supervision, Investigation, Formal analysis. **Naurang L. Saini:** Writing – review & editing, Writing – original draft, Visualization, Validation, Supervision, Resources, Project administration, Methodology, Investigation, Formal analysis, Data curation. **Aichi Yamashita:** Writing – review & editing, Validation, Supervision, Resources, Project administration, Methodology, Investigation, Formal analysis, Data curation, Conceptualization. **Akira Miura:** Writing – review & editing, Supervision, Investigation, Formal analysis. **Muammer**

Yasin Hacisalihoglu: Writing – review & editing, Validation, Supervision, Methodology, Investigation, Formal analysis, Data curation. **Hiroto Arima:** Writing – review & editing, Validation, Supervision, Methodology, Investigation, Formal analysis, Data curation, Conceptualization. **Giovanni Tomassucci:** Writing – review & editing, Validation, Supervision, Methodology, Investigation, Formal analysis, Data curation.

Declaration of Competing Interest

The authors declare the following financial interests/personal relationships which may be considered as potential competing interests: Yoshikazu Mizuguchi reports financial support was provided by Japan Society for the Promotion of Science. If there are other authors, they declare that they have no known competing financial interests or personal relationships that could have appeared to influence the work reported in this paper.

Acknowledgements

The authors thank O. Miura for supports in experiments. This work was partly supported by JSPS-KAKENHI (23KK0088), TMU Research Project for Emergent Future Society, and Tokyo Government-Advanced Research (H31–1). This work has been done under bilateral agreement between Tokyo Metropolitan University and Sapienza University of Rome.

Appendix A. Supporting information

Supplementary data associated with this article can be found in the online version at doi:10.1016/j.jallcom.2024.177442.

Data availability

Data will be made available on request.

References

[1] Z. Fisk, R. Viswanathan, G.W. Webb, Solid State Commun. 15 (1974) 1797–1799.
[2] B.T. Matthias, E. Corenzwit, Phys. Rev. 100 (1955) 626–627.
[3] J. Lefebvre, M. Hilke, Z. Altounian, Phys. Rev. B 79 (2009) 184525.
[4] A. Teruya, M. Kakihana, T. Takeuchi, D. Aoki, F. Honda, A. Nakamura, Y. Haga, K. Matsubayashi, Y. Uwatoko, H. Harima, M. Hedo, T. Nakama, Y. Ōnuki, J. Phys. Soc. Jpn. 85 (2016) 034706.
[5] K.J. Syu, S.C. Chen, H.H. Wu, H.H. Sung, W.H. Lee, Phys. C. 495 (2013) 10–14.
[6] M. Takekuni, H. Sugita, S. Wada, Phys. Rev. B 58 (1998) 11698–11702.
[7] Z. Henkie, W.A. Fertig, Z. Fisk, D.C. Johnston, M.B. Maple, J. Low. Temp. Phys. 48 (1982) 389–403.
[8] K. Yamaya, T. Sambongi, T. Mitsui, J. Phys. Soc. Jpn. 29 (1970) 879.
[9] Y. Watanabe, H. Arima, H. Usui, Y. Mizuguchi, Sci. Rep. 13 (2023) 1008.
[10] C. Tayran, M. Çakmak, Physica B, Condens. Matter 661 (2023) 414904.
[11] Y. Mizuguchi, M.R. Kasem, Y. Ikeda, J. Phys. Soc. Jpn. 91 (2022) 103601.
[12] H. Arima, M.R. Kasem, Y. Mizuguchi, Appl. Phys. Express 16 (2023) 035503.
[13] M.R. Kasem, H. Arima, Y. Ikeda, A. Yamashita, Y. Mizuguchi, J. Phys. Matter 5 (2022) 045001.
[14] M. Xu, Q. Li, Y. Song, Y. Xu, A. Sanson, N. Shi, N. Wang, Q. Sun, C. Wang, X. Chen, Y. Qiao, F. Long, H. Liu, Q. Zhang, A. Venier, Y. Ren, F. d'Acapito, L. Olivi, D.O. De Souza, X. Xing, J. Chen, Nat. Commun. 14 (2023) 4439.
[15] Y. Mizuguchi, Md.R. Kasem, T.D. Matsuda, Mater. Res. Lett. 9 (2021) 141–147.
[16] M.R. Kasem, A. Yamashita, T. Hatano, K. Sakurai, N. Oono-Hori, Y. Goto, O. Miura, Y. Mizuguchi, Supercond. Sci. Technol. 34 (2021) 125001.
[17] E. Batalla, Z. Altounian, J.O. Strom-Olsen, Phys. Rev. B 31 (1985) 577.
[18] Z. Altounian, J.O. Strom-Olsen, Phys. Rev. B 27 (1983) 4149–4156.
[19] G.R. Stewart, Adv. Phys. 66 (2017) 75–196.
[20] S. Kawaguchi, M. Takemoto, K. Osaka, E. Nishibori, C. Moriyoshi, Y. Kubota, Y. Kuroiwa, K. Sugimoto, Rev. Sci. Instrum. 88 (2017) 085111.
[21] F. Izumi, K. Momma, Solid State Phenom. 130 (2007) 15–20.
[22] K. Momma, F. Izumi, J. Appl. Crystallogr. 41 (2008) 653–658.
[23] L.N. Cooper, J. Bardeen, J.R. Schrieffer, Phys. Rev. 108 (1957) 1175.
[24] W.L. McMillan, Phys. Rev. 167 (1968) 331–344.
[25] A.M. Clogston, Phys. Rev. Lett. 9 (1962) 266–267.
[26] B.S. Chandrasekhar, Appl. Phys. Lett. 1 (1962) 7.
[27] A. Kreyssig, M.A. Green, Y. Lee, G.D. Samolyuk, P. Zajdel, J.W. Lynn, S.L. Bud'ko, M.S. Torikachvili, N. Ni, S. Nandi, J.B. Leão, S.J. Poulton, D.N. Argyriou, B. N. Harmon, R.J. McQueeney, P.C. Canfield, A.I. Goldman, Phys. Rev. B 78 (2008) 184517.
[28] A. Van Roekeghem, P. Richard, X. Shi, S. Wu, L. Zeng, B. Saparov, Y. Ohtsubo, T. Qian, A.S. Sefat, S. Biermann, H. Ding, Phys. Rev. B 93 (2016) 245139.
[29] D. Guterding, S. Backes, H.O. Jeschke, R. Valentí, Phys. Rev. B 91 (2015) 140503.
[30] A. Ptok, K.J. Kapcia, M. Sternik, P. Piekarz, J. Supercond. Nov. Magn. 33 (2020) 2347–2354.
[31] P.G. Naumov, K. Filsinger, O.I. Barkalov, G.H. Fecher, S.A. Medvedev, C. Felser, Phys. Rev. B 95 (2017) 144106.
[32] R.S. Dhaka, R. Jiang, S. Ran, S.L. Bud'ko, P.C. Canfield, B.N. Harmon, A. Kaminski, M. Tomić, R. Valentí, Y. Lee, Phys. Rev. B 89 (2014) 020511.
[33] A. Ptok, M. Sternik, K.J. Kapcia, P. Piekarz, Phys. Rev. B 99 (2019) 134103.